Applied Physics Research; Vol. 16, No. 1; 2024
ISSN 1916-9639 E-ISSN 1916-9647
Published by Canadian Center of Science and Education

Dual-Sided Rotor Design for Performance Boost of Synchronous Reluctance Motors in Electric Vehicles

Luis Teia[1]

[1] von Karman Institute for Fluid Dynamics, Chaussée de Waterloo 72, 1640 Rhode-Saint-Genèse, Belgium

Correspondence: Dr Luis Teia, von Karman Institute for Fluid Dynamics, Chaussée de Waterloo 72, 1640 Rhode-Saint-Genèse, Belgium. E-mail: luisteia@sapo.pt

Received: October 21, 2023 Accepted: December 6, 2023 Online Published: February 7, 2024
doi:10.5539/apr.v16n1p20 URL: https://doi.org/10.5539/apr.v16n1p20

Abstract

Increasing environmental awareness is pushing the design of electic motors to favor none rare-earth solutions (i.e., without permanent magnets), and one such example is the SyncRM 2 (or concentrated-coiled SRM2) being proposed for the electric hybrid automobile Toyota Yaris. Following on an already established line of research on this topic, this article proposes a new design that re-assigns most of the magnetic material in the stator to the rotor — resulting in the Dual-sided SyncRM (a variant of the SRM2). The detrimental effect (caused by the extra gap) of slightly reducing the aligned inductance is overwhelmingly outweighed by the beneficial effect of drastically reducing the unaligned inductance. Extensive back-to-back FEMM analysis was conducted, where the recomputed SRM2 matches previous research, providing confidence to the favorable predictions of the Dual-sided SyncRM. Both performances are compared, with the venue being available for download on an open-source database. A realistic photo-rendered three-dimensional model is displayed and also available. An important outcome is the Dual-sided SyncRM torque (and power) increased by 29% (with respect to the SRM2), achieving a saliency ratio of 10 and an efficiency boost to 91% (at the rated operational speed of 1200rpm).

Keywords: switched reluctance motor, magnetic FEM, analytic method, torque, power, efficiency

The hybrid vehicle Toyota Yaris (Figure 2a) runs on an electric motor possessing permanent magnets (Figure 2b) [Takeno et al, 2012]. There is a contemporary global effort to reduce the usage of rare-earth materials that has fueled research to find alternative solutions. A recent effort resulted in the formulation of an alternate design (Figure 2c) that uses solely the reluctance torque effect to operate [the Synchronous Reluctance Motor 2, or SRM2 as defined by Takeno et al (2012)]. Upon numerical simulations and experimental tests, this was proven to be an effective solution. Then building on this foundation, Stuikys and Sykulski (2020) created an effective and traceable low-order model (assisted by FEM magnetic numerical modeling) that predicted the SRM2 performance with impressive accuracy.

Figure 1: (a) The hybrid automobile Toyota Yaris, (b) its electric motor and (c) a possible SyncRM alternative

Continuing on this approach, the present article builds on this collective research effort, and uses this low-order model to modify the stator and rotor design towards boosting its torque, power and efficiency. Over the past 50 years, research studies (Menzies 1972, Landislav et al 2020, Ionel and Popescu 2011) involving SR motors designed them such that the stator's magnetic mass was equivalent (or larger) than that of the rotor. This over unity stator-to-rotor mass ratio greatly influences the magnetic circuit impedance response, as the rotor turns between the aligned to the unaligned cases, and consequentially its performance.

1. Hypothesis

A larger co-energy production (and thus torque/power per motor step rotation) is potentially achievable by minimizing the mass portion of magnetic conductor in the stator (that is, by re-assigning this mass to the rotor), such that the impedance when the rotor is unaligned is dramatically reduced (with an acceptable collateral reduction of the aligned impedance).

2. Theory

The SRM2 is a radial flux synchronous reluctance motor possessing at the center an aluminium shaft, a steel rotor with 18 physical poles, and a surrounding steel stator with 12 physical poles (Figure 2a). The gap between the stator and rotor is 0.5mm wide. Each stator pole has concentrated coils composed of twenty two sets of 17 parallel connected turns of AWG wire with 0.6mm internal diameter. They are driven by a three-phased electric bus controlled via a Pulse-Width Modulation (PWM) scheme (characteristic for this type of motor). This means that sets of 6 coils disposed in a hexagonal manner are driven by one of the phases, creating six electromagnetic poles that (with alternation from one phase to the next) creates the effect of a rotating magnetic field. The rotor cavities between the stator and rotor are filled with air, as is the surroundings of the motor/stator (representing an important boundary condition to be implemented later during the numerical analysis).

The proposed design modification (hereafter termed Dual-sided SyncRM shown in Figure 2b) circumferential splits the stator at the radially outer extremity of the windings, and re-assigns that outer part of the magnetic circuit to the rotor (which is hence forth termed the rotor outer ring). This has the consequence of generating an outer gap (in addition to the inner gap), and of making the motor slightly bigger (i.e., the outer diameter increased). However, the modification of the motor did not affect its inner dimensions, that is the diameter of the shaft remains the same, and so does the (now termed) rotor inner ring (where before, it was just the rotor in Figure 2a), the size and locations of the windings is also the same, and so is the location and size of the stator poles. It is worth mentioning that the modified design is just a first attempt that is by no means optimized; there is plenty of room for improvement. It is assumed that the Dual-sided SyncRM will operate via the same power bus and PWM-controller scheme as the SRM2 [for further details, please see Stuikys and Sykulski (2020)].

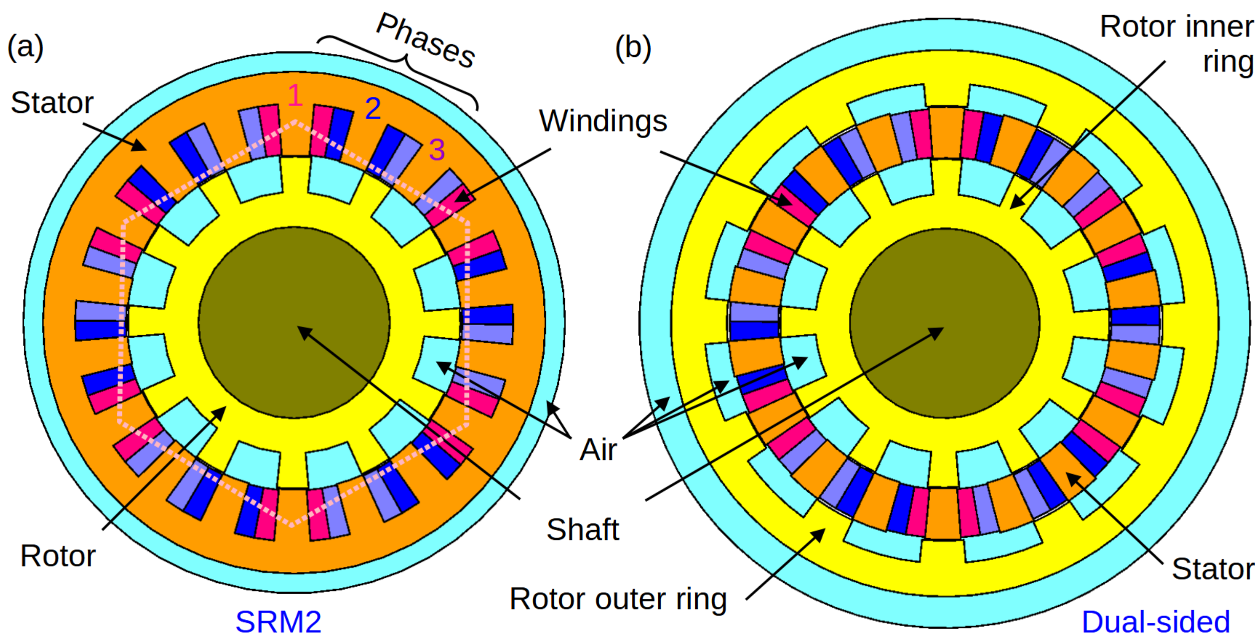

Figure 2: Axial midplane cut-out of (a) SRM2 and (b) Dual-sided SyncRM

A 3D model of the Dual-sided SyncRM is shown in Figure 3, and available (FCStd1, Step, Stl) to download here at this author's open profile page. This was built with the open-source software FreeCAD, and professionally photo-rendered using the open-source software CADrays. It's key characteristics are now briefly explained. The stator is composed of a rear structural disc-like feature that fixes onto the vehicle interface, and to which (on the other side) the poles are connected (Figure 3a). In turn, these stator poles slide inside the Dual-sided rotor, in itself composed of an inner and outer ring linked by structural connectors. The windings are virtually the same as the SRM2, with slight modifications being made at each extremity (necessary to hold the windings in place). As shown in the zoom at the lower left corner of Figure 3a, the individual wires are turned around the open slot/gap at the front end and at the closed slot/gap at the back. These prevent the wires from rising above the inner and outer surface of the stator pole (which would result in a clash with the rotor), allowing the rotor to turn freely.

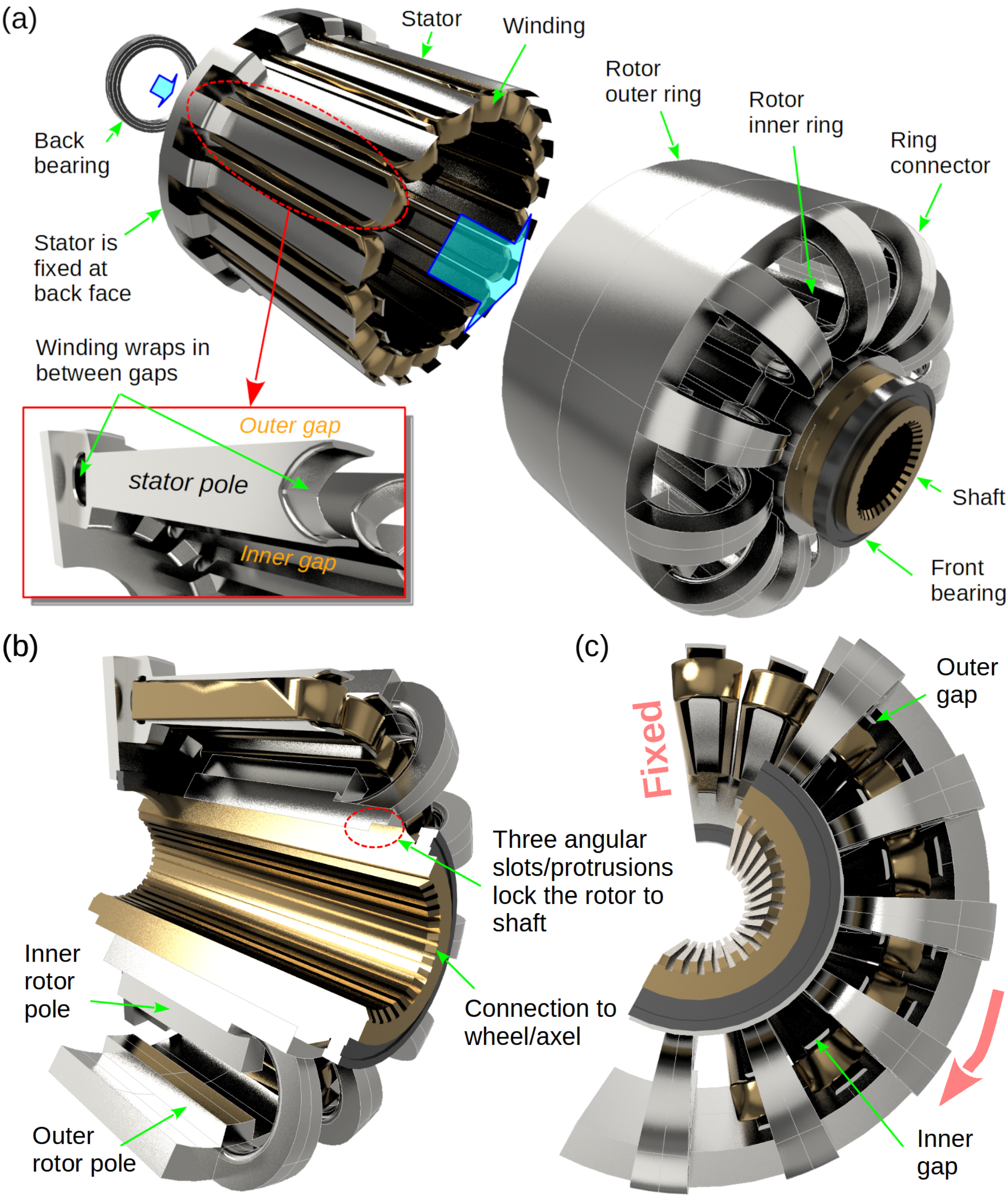

Figure 3: Dual-sided SyncRM: (a) assembly perspective view, (b) cut-out perspective view and (c) cut-out front view

A back bearing (Figure 3a left) connects the (fixed) rear disc-like feature of the stator to the shaft (that is, the outer surface of the bearing is fixed from rotating, and the inner surface turns with the shaft) [this is more readily visible at the back of the half model in Figure 3b]. A front bearing provides the second support for the shaft (and thus also to the rotor). Similarly, the outer surface of the front bearing connects to a fixed structure of the vehicle. The rotor is geared to the shaft (via three angularly equidistant slots on the rotor that slide into three corresponding angular protrusions on the shaft — visible on Figure 3b). The rotor transmits its loads to the shaft, that in turn drives the wheel and/or axle (to which is connected via the inner teeth) [as the half model front view in Figure 3c illustrates]. From a manufacturing perspective, and while it may be complex to execute, it is entirely possible to machine the Dual-sided rotor as a single piece via a series of combined axial translation and rotational cuts. Alternatively, the single piece could be manufactured first via casting, which would be followed by precise machining of the critical surfaces (i.e., the cylindrical inner surface interface to the shaft and the poles' surfaces interfacing the inner and outer gaps) to the required precision. If extra stiffness (to the stator poles) is required, the tip of the stator poles can be connected via a ring (not shown in Figure 3), where care must be taken for this new ring not to interfere with the rotor. Making both the rotor and stator as single pieces makes it is easier to control the tolerances required to achieve the tight gaps, both radially inner and outer. Achieving the necessary gap width during assembly and operation is priority, and to that effect, the physical geometry of the support connectors in the rotor can (if necessary) be made of another shape (e.g., with angled corners) if it proves to be more convenient for manufacture.

3. Analysis Method

The impact of the modified design on motor performance is computed using the approach provided by Stuikys and Sykulski (2020), encompassing a new low-order model applicable to any generic radial-flux SyncRM. Several reasons lead to this choice. One reason is that by using vector theory, the area of the quadrilateral between the aligned and unaligned flux-linkage responses (to changing operating current) determines directly the conversion energy W', which in turn translates into reluctance torque and electromagnetic power (this is further explained later in the Results section). Another reason is that this method is validated against experimental data provided by Takeno et al (2012), which yielded a good correlation. Moreover, it is well documented and clearly traceable (making it transparent), allowing identification of how it works and of its limitations. To this effect, the present research charted numerically the flux-linkage performance, both for the original SRM2 (Figure 4a) and novel Dual-sided SyncRM (Figure 4b). The planar electromagnetic simulation of the motor was conducted using the open-source software FEMM, with the motor cross section drawn using the open-source software NanoCAD (Arslan, 2021). Each mesh comprise of $\sim$ 35500 cells for the SRM2 and $\sim$ 48400 cells for the Dual-sided SyncRM. Simulations were conducted for various rotor angular positions, namely 0, 2, 4, 6, 8, 10, 12 and 15 degrees (between stator and rotor pole axis). The results are available as DWG and FEMM files for download at this author's profile page on the open-source platform Figshare, for both the SRM2 and the Dual-sided SyncRM.

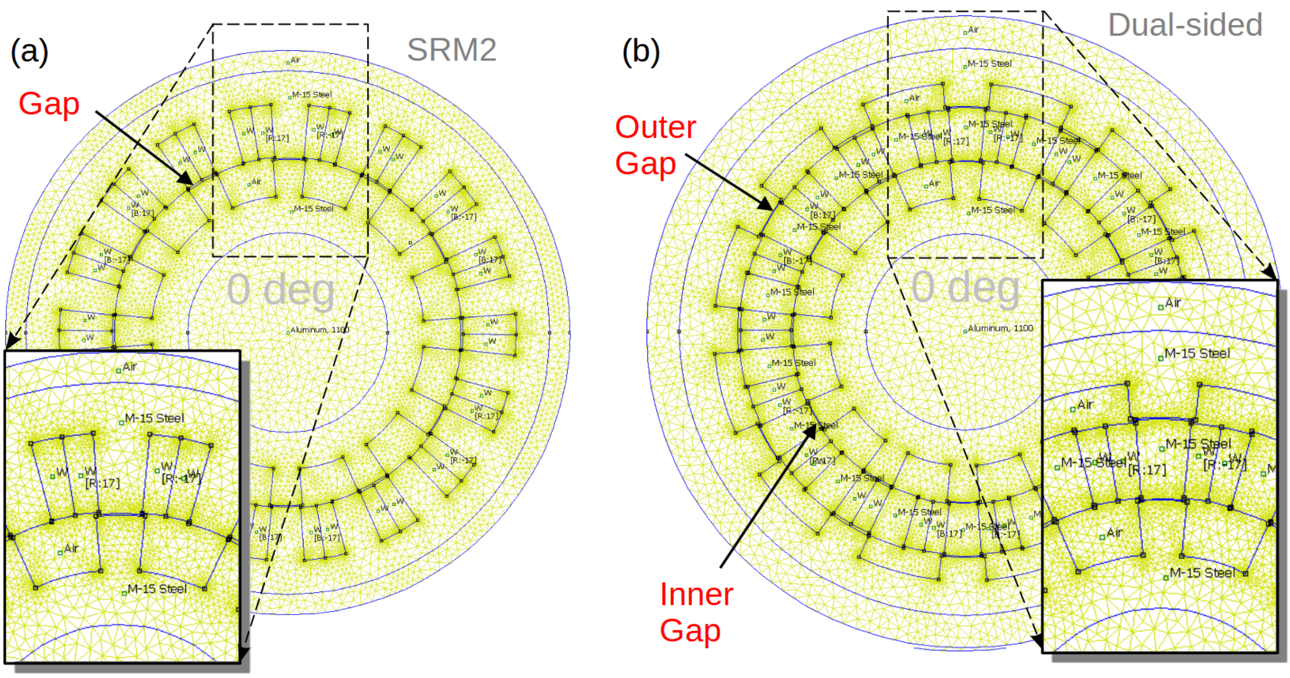

Figure 4: FEMM mesh for the (a) SRM2 and (b) Dual-sided SyncRM

The motor depth was set (at the FEMM "Problem definition" menu) identical to that of the SRM2 (or 135mm) [1,2], allowing for a compliant comparison between the two machines. Material seeds were added to each corresponding region. Practically all the materials necessary for the calculations were found in the FEMM software library, except for the wire which had to be adapted via a simple modification to the existing AWG wires. The SRM2 had each stator pole coiled with 17 parallel-connected wires (each with a diameter of d=0.6mm) with 22 turns (around the pole) each, stacked on top of each other. The approach used to model this in FEMM was to lump the 22 turns into a single turn of an equivalently larger diameter wire ($D = \sqrt{N} \times d = \sqrt{22} \times 0.6 \approx 3mm$, having the same group crossectional area and thus transporting the same current —- skinning effects are not considered here), and coil it 17 times around the pole. An electrical circuit named "R" was created and assigned to the wiring region at either side of the top dead center physical stator pole. The left side presents the positive (into the page) bundle of 17 modified AWG wires (connected in series), while the right side presents the negative (out of the page) portion of those same 17 modified wire bundles. Since in this simulation only phase 1 is active (refer back to Figure 2a), the remainder wires (of phase 2 and 3) were assigned the same wire material but without any circuit. Unfortunately, at the time of creation of this research, data on the steel 10JNX900 (Misao et al, 2005) was not known. Instead, steel M-15 was used (for both the stator and rotor), as it was readily available in the FEMM library [for additional information on steel M-15, see for example AKSteel (2007)]. As a follow-on work, the high performance steel reference 10JNX900 [Youyou Technology Co. Ltd, 1993] (used for the original SRM2 motor) could be programmed into the FEMM files [most importantly the B-H curve — for more information see the example of Wakisaka et al (2013)] and assigned as a new rotor-stator material for a rerun, and subsequent comparison to the results from this research. In turn, the lightweight and structurally-strong non-magnetic material aluminium 1100 is used for the shaft. As a boundary condition, a region of air was added to the outer diameter of the stator (providing the magnetic insulation of the stator from the rest of the environment). Seeds of the material Air were also allocated to the cavities in between the rotor and the stator, including their inner and outer gaps. Similarly to the SRM2, the width of both inner and outer air gaps were set to 0.5 mm each. Additional key dimensions of the motors are as follows: Stator outer diameter is 234.5mm, while the inner diameter is 178.9mm. The rotor outer diameter is 296mm and inner diameter 102.6mm. It is likely that the magnetic flux-linkage (a parameter critical to determine the Co-Energy W') is being computed (by FEMM) via following the flux lines until they close a loop, following by integrating along that path [as explained in Guilera (2018)]. This is done for each circuit ("R" being one already mentioned, and another called "B"), resulting in the values exported from the software. The total flux-linkage Ψ of the motor is the sum of those computed for each circuit (i.e., "R" plus "B").

4. Results

The Magnetic Field Intensity B distribution within stator and rotor for both motors are shown as color plots in Figure 5. The predicted magnetic loops (in Figure 5) are clearly seen all around the rotor-stator assembly. High regions of flux are observed around the coils, with the flux direction alternating as expected between each of the six rotor segments. Comparing the aligned cases of the SRM2 (Figure 5a) and the Dual-sided SyncRM (Figure 5b) shows that the flux density is maintained high at the stator pole and inner rotor pole in both cases, but drops visibly (radially immediately after the stator pole) because of the introduction of the new (outer) gap. This drop is to be expect since air has a much lower magnetic permeability than steel. Therefore, qualitatively the extra gap is expected to have a noticeable impact on the induction for the aligned case. However, comparing the flux intensity for the unaligned cases between the SRM2 (Figure 5c) and the Dual-sided SyncRM (Figure 5d) shows that first is much higher. This occurs because for the Dual-sided SyncRM the source of magnetism (i.e., the stator pole) is now much more isolated from the rest of the magnetic material, resulting in a substantial reduction in induced magnetic flux on all of the steel material (both rotor and stator). That is, the magnetization effect from the coils is much more isolated, and thus weak. Qualitatively, this isolation of the stator poles is expected to have a substantial impact on the overall induction for the unaligned case. Quantitatively, the performance of both the SRM2 and Dual-sided RM is calculated by applying the method from Stuikys and Sykulski (2020), which is now explained. The total electromagnetic power P provided by torque T at a rated angular speed ω is given as

$$P = T \times \omega \qquad \text{with} \qquad T = \left(W' \times \frac{q.N_r}{2\pi}\right) \times R \tag{1}$$

where N_r is the number of physical poles of the rotor, and q is the number of electric phases. The factor R removes the overlap between subsequent rotational unaligned-aligned segments (where the electrical input switches sequentially between the 3 phases), being defined as a factor dependent on the segment angle β_s, the number of stator poles N_s and the number of rotor poles N_s, resulting in

$$R = 1 + \frac{1}{\beta_s}\left[\beta_s - \left(\frac{360}{N_r} - \frac{360}{N_s}\right)\right] = 1 + \frac{1}{10.5}\left[10.5 - \left(\frac{360}{12} - \frac{360}{18}\right)\right] = 1.0476 \tag{2}$$

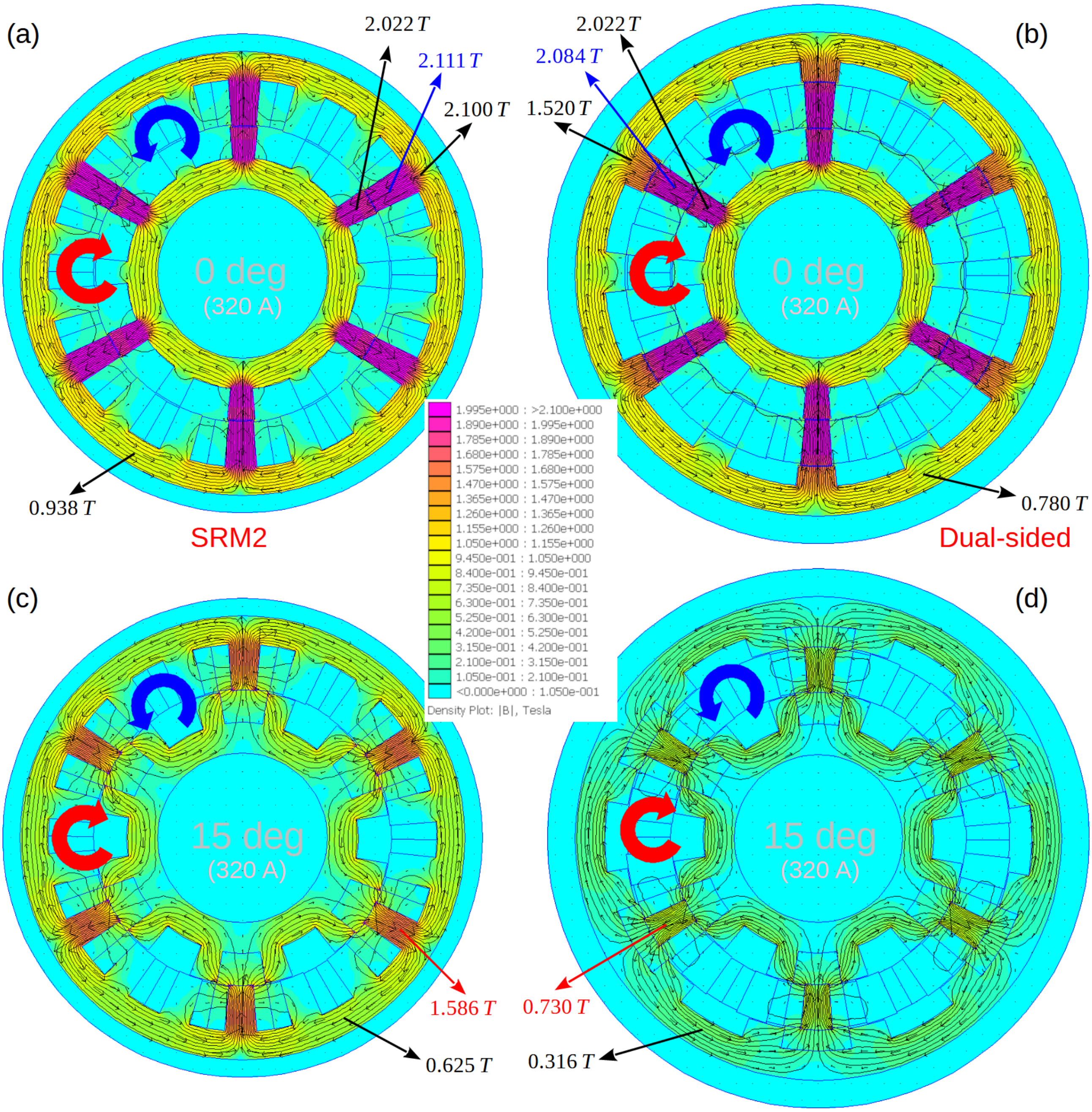

Figure 5: Magnetic flux distribution for the [0 deg] (a) SRM2 and (b) D-SRM; and [15 deg] (c) SRM2 and (d) D-SRM

The magnetic co-energy W' is computed from the mapping of flux-linkage response (as the rotor transits from unaligned to aligned to the stator) for varying electrical current. In fact, the co-energy is the area in between the response lines from the completely unaligned to completely aligned cases. The previous qualitative magnetic flux density change with stator-rotor alignment in Figure 5 (for both motors) are now seen quantitatively in Figure 6 (for a wider range of rotor angles and currents). Figure 6a shows the flux-linkage Ψ response (a parameter directly proportional to the flux density ϕ at the stator pole) for varying rotor mechanical angle for the SRM2, and Figure 6b for the Dual-sided SyncRM). Both cases present a similar response, in that a maximum is observed when aligned (i.e., 0 deg) that gradually reduces towards unalignment (i.e., towards 15 deg), where current plays in general an amplification effect of the response. As noted earlier, the fact that the Dual-sided SyncRM breaks the magnetic circuit on either side of the windings (effectively isolating them during unalignment), makes the drop in flux-linkage in the unaligned angles (in Figure 6b) much more pronounced than with respect to SRM2 (in Figure 6a). Figure 6c shows the flux-linkage Ψ response for varying current for SRM2, and Figure 6d for Dual-sided SyncRM. This is the same data as in Figures 6a and 6b, except they are plotted for varying current — this will be more usefull when later we compute electromagnetic torque and power. In Figures 6c and 6d, both motors present a linear response up to a current of about 80A, where the steepness of the response is very much dependent on the stator-rotor alignment. However, most engines operate at much higher currents than 80A (the SRM2 operates at a rated current of 320A)[Takeno et al 2012, Stuikys and Sykulski 2020]. Beyond 80A, the effect of magnetic saturation starts to appear, resulting in a non-linear response (which is connected to the non-linear B-H curve inherent to the selected magnetic material for the stator and rotor) — a non-linear effect that becomes more pronounced as the rotor aligns with the stator (i.e., when the magnetic flux density intensifies). Note that the proposed design modification has substantially reduced the inclination of the linear response for the unaligned case (i.e., 15 deg) from the SRM2 (lowest line in Figure 6c) to the Dual-sided SyncRM (lowest line in Figure 6d).

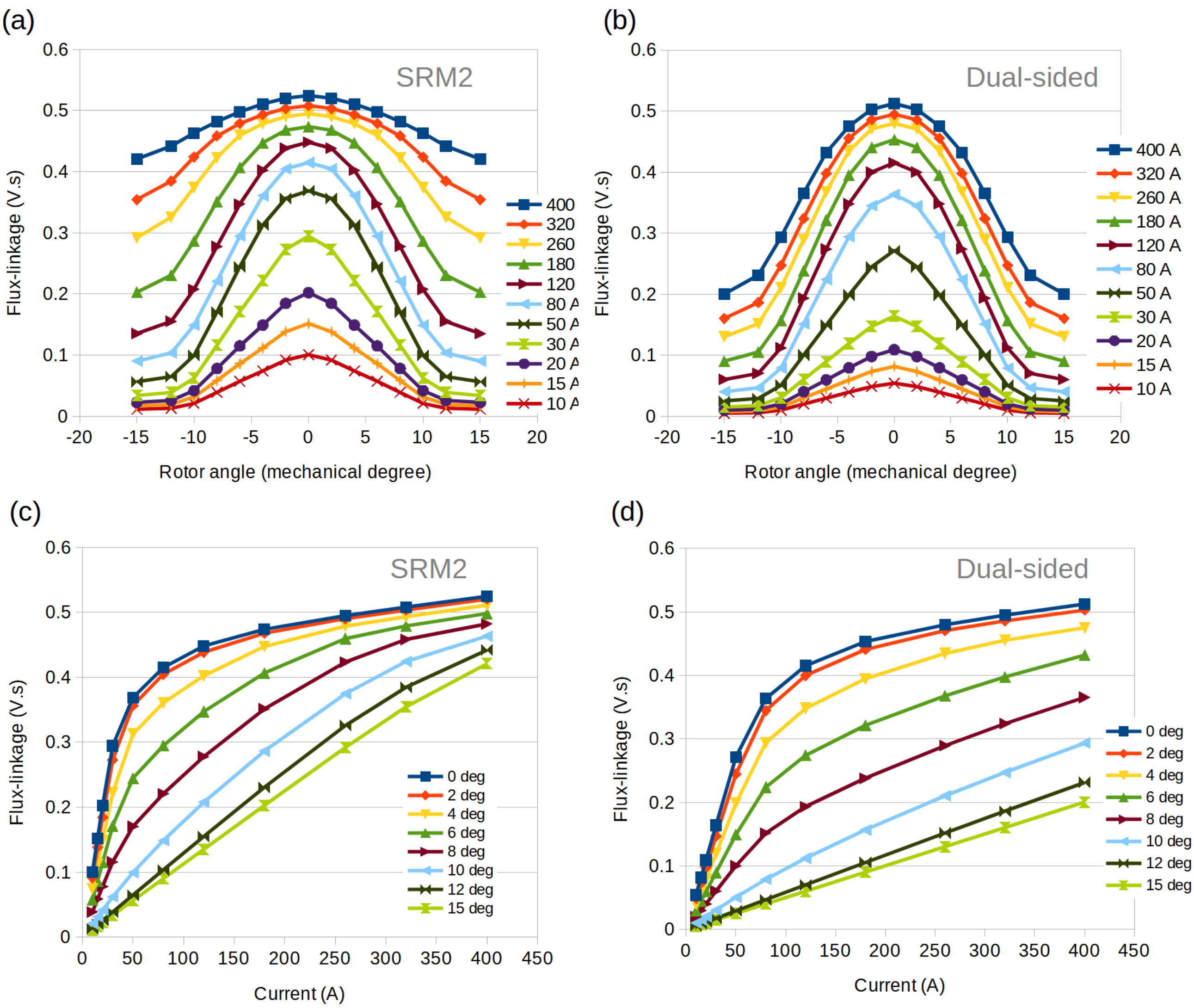

Figure 6: Flux-linkage map [versus mechanical angle] (a) SRM2 and (b) Dual-sided; and [versus current] (c) SRM2 and (d) Dual-sided

Computation of the Co-Energy W' requires only accounting the response from the extreme cases [i.e., when the rotor is aligned (0 deg) and unaligned (15 deg)], as previously shown in Figure 6c for SRM2 and Figure 6d for Dual-sided SyncRM. From a practical perspective, subsequent analysis requires these sets of two lines to be replotted in Figure 7, one set for SRM2 (in black) and another for Dual-sided SyncRM (in red). From this raw data (in Figure 7), additional pertinent information on motor performance can be extracted. To make a distinction on what information belongs to which motor, the parameters associated with the Dual-sided SyncRM have henceforth an apostrophe at the end (all others, including those that are both common to the two motors and that pertain solely to SRM2, do not have this apostrophe). Disregarding commutation for now (i.e., disregarding the effect of reducing current prior to stator-rotor pole alignment, thus preventing negative torque), it can be seen that the design modification has substantially increased the conversion energy from the SRM2 (i.e., the black area W'_{SRM2} delimited by the quadrilateral $OABD$) into that of the Dual-sided SyncRM (i.e., the red area W'_{Dual-S} delimited by the quadrilateral $OA'B'D'$). The slight reduction in area caused by the (extra) radially outer gap (i.e., the area $ODBB'D'$) is superseded by the larger increase in area caused by the reduced unaligned induction of the magnetic circuit (i.e., the area $OA'A$). Prior to magnetic saturation in the stator and/or rotor, the flux-linkage response to increasing current is practically linear (as shown by lines OD for SRM2 and OD' for Dual-sided SyncRM). When saturation occurs (at around 80A in SRM2), the slope reduces drastically presenting a non-linear response. This is to be expected from the definition of flux-linkage $\Psi = N.\phi$, where N is the number of coils around the stator and ϕ is the magnetic flux density, reflecting the B-H curve behavior of the stator/rotor ferromagnetic material [being for steels tipically non-linear (Wakisaka et al 2013, YouYou Technology Co. Ltd. 1993)]. Linear trendlines were ploted for each of the three cases, both for the SRM2 (in black) and for the Dual-sided SyncRM (in red), including the respective equations and R^2 levels of confidence. The inclination of each trendline is — by definition — the inductance value L for each stator-to-rotor position, namely for example the Dual-sided SyncRM: L'_{uu} for when the circuit is unsaturated and the rotor is unaligned, L'_{ua} when unsaturated and aligned, and finally L'_{sa} when saturated and aligned.

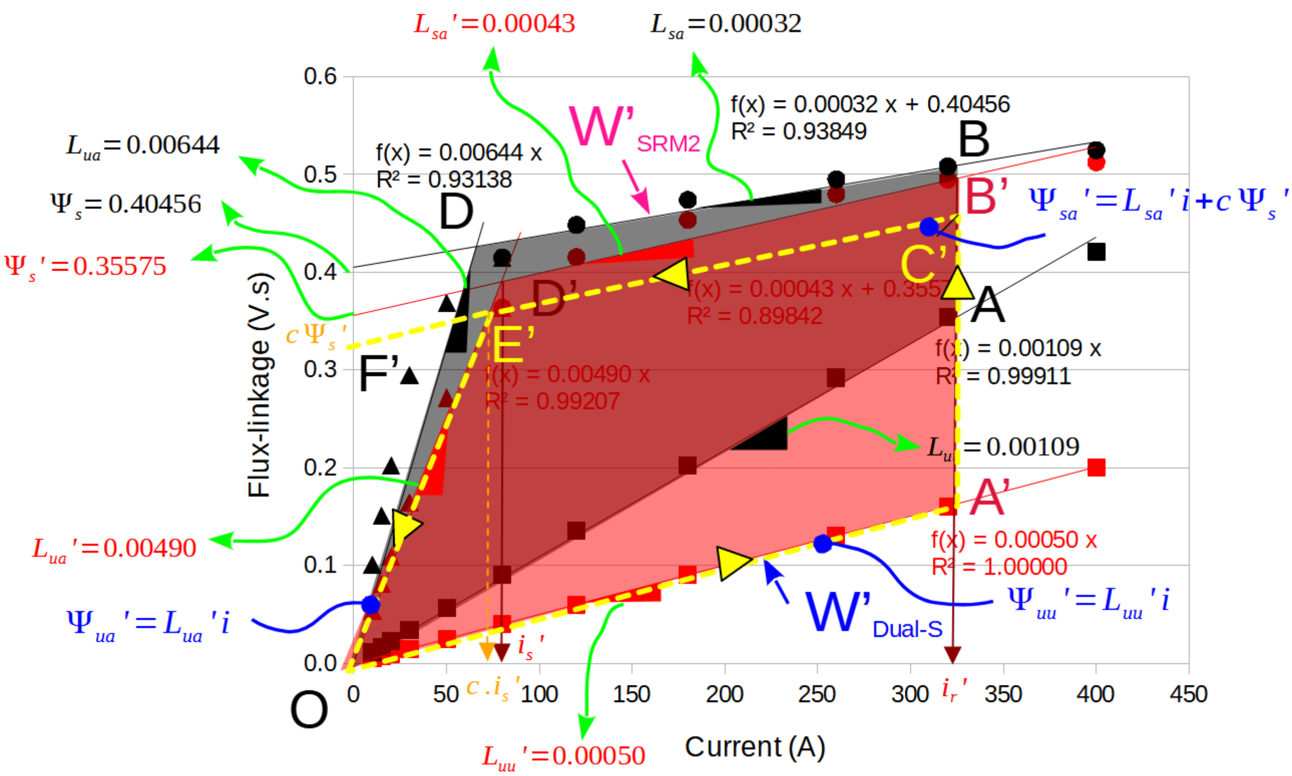

Figure 7: Co-energy assessment for both the SRM2 (in black) and Dual-sided SyncRM (in red)

However, commutation is typically employed to avoid unwanted production of negative torque. Thus, for the Dual-sided SyncRM the rotation of the rotor through an angular sector is described (in Figure 6) by the yellow dashed lines with vectorial path $OA'C'E'$ (instead of the uncommuted path described by lines surrounding the red area $OA'B'D'$). That is, for the Dual-sided SyncRM, the rotor path starts at point O in a completely unaligned state, being followed by a ramp-up towards the rated current i_r. Then this constant rated current is applied for a period of time, during which the unaligned magnetic circuit drives the rotor to rotate further. As the rotor pole approaches alignment with the stator pole, the current starts to reduce, and commutation occurs at point B' (instead at point B, where it would be completely aligned). If the rated current i_r acted all the way until the rotor was fully aligned with the stator, then instead the Dual-sided SyncRM would follow the path $OA'B'D'$, and in the case of the SRM2 it would follow the path $OABD$. According to Eq.(1), in order to proceed with the computation of the produced torque and EM power it is necessary to compute the Co-Energy W' (i.e., the commuted area in the general quadrilateral $OA'C'E'$ in Figure 7 for the Dual-sided SyncRM), which is determined via the mathematical application of vector theory. A brief summary is now given. Vector theory (Shapiro and de Berredo-Peixoto, 2013) states that the area of a general quadrilateral with vertices $(x_1, y_1) = (0,0)$, $(x_2, y_2) = (i_r, \Psi_{uu})$, $(x_3, y_3) = (i_r, \Psi_{sa})$ and $(x_4, y_4) = (i_s, \Psi_{ua})$ [listed counterclockwise along its perimeter] is given by

$$W' = \frac{1}{2}\left\{\begin{vmatrix} 0 & i_r \\ 0 & \Psi_{uu} \end{vmatrix} + \begin{vmatrix} i_r & i_r \\ \Psi_{uu} & \Psi_{sa} \end{vmatrix} + \begin{vmatrix} i_r & i_s \\ \Psi_{sa} & \Psi_{ua} \end{vmatrix} + \begin{vmatrix} i_s & 0 \\ \Psi_{ua} & 0 \end{vmatrix}\right\} = \frac{1}{2}\left\{i_r\left(\Psi_{ua} - \Psi_{uu}\right) - \left(i_s - i_r\right)\Psi_{sa}\right\} \quad (3)$$

where the matrices in between the modulus are determinants, solved to be equal to the subtraction of the cross-products. Expanding this (by replacing the flux-linkage definitions Ψ_{ua}, Ψ_{uu} and Ψ_{sa} in Figure 7) gives

$$W' = \frac{1}{2}\left\{(L_{sa} - L_{uu})i_r^2 + (L_{ua} - L_{sa})i_r i_s + c\Psi_s i_r - c\Psi_s i_s\right\} \tag{4}$$

Careful observation of Figure 7 shows that the saturation current i_s is deduced as

$$i_s = \frac{\Psi_s}{L_{ua} - L_{sa}} = \frac{0.35575}{0.0049 - 0.00043} = 79.6A \tag{5}$$

According to Stuikys and Sykulski (2020), Eq. (4) can be further expanded to become a function of angles, voltages, currents and inductances, as

$$W' = \frac{1}{2}\left\{2.V_{rms(PWM)}\frac{c.\beta_s}{\omega}.i_r + (L_{uu} - L_{sa})i_r^2 - \frac{(V_{rms(PWM)}\frac{c.\beta s}{\omega} + (L_{uu} - L_{sa}).i_r)^2}{L_{uu} - L_{sa}}\right\} \tag{6}$$

For a designer of electric motors, Eq.(6) can be used for example to perform sensitivity studies, or to taylor the machine to a specific torque and/or power requirement. For those who wish to understand and improve this method, here is a brief explanation on how this method was derived. For additional details, please refer to their original publication. The present author started by applying Eq.(6) to the reconstructed 2D CAD model of the original SRM2, which gave a very close approximation of the results given by Stuikys and Sykulski (2020) [summarized later in Table 1, which can be compared by referring to their original article]. Upon re-application and verification of this method to the baseline SRM2, it was subsequentially applied to the Dual-sided SyncRM, with the key calculations for the later being presented below. The target rotational speed of the original SRM2 is 1200 rpm, which for a machine with $N_r = 12$ physical rotor poles gives

$$f = \frac{\text{rpm} \times \text{number of poles}}{120} = \frac{1200 \times 12}{120} = 60Hz \tag{7}$$

The argument could be done inversely, in that for a target operating mains frequency of 60Hz, and a SR motor with 12 physical rotor poles, the operational rpm will be 1200. In radians per second, this translates to a rotational speed ω of

$$\omega = \frac{1200}{60} \times 2\pi = 125.7rad/s \tag{8}$$

The computation of the commutation angle takes advantage of the fact that the unit of flux-linkage, the Weber, is also expressible as Volts-second, which provides (in conjunction with the angular speed ω) a direct bridge between the angular position of the rotor θ and the magnitude of the flux-linkage Ψ. Thus, Figure 9 suggests that the commutation angle θ_{CE} is equivalent to the time taken for the current to fall from point C' to E' (a vertical flux-linkage drop equal — but offset — to that from point B to D) [this may be difficult to vizualize now, but it will become cleared later when analyzing Figure 9] . This flux-linkage vertical drop occurs at an angular rotation ω and bus voltage V_{DC}, resulting in

$$\theta_{CE} = \left[\frac{\Psi_{sa}(@B) - \Psi_{sa}(@D)}{V_{DC}}\right] \times \omega = \left[\frac{0.49335 - 0.389972}{500}\right] \times 125.7 = 1.49deg \tag{9}$$

Another important parameter to compute is the commutation factor c, which is a multiplier coefficient that accounts for the aforementioned period of ramping down of the current (from point C' to E') in the $OA'C'E'$ cycle, and is given as

$$c = 1 - \frac{\theta_{CE}}{\beta_s} = 1 - \frac{1.49}{10.5} = 0.86 \tag{10}$$

The rms voltage $V_{rms(PWM)}$ (across the windings) necessary to counteract the back-electromotive force (at the rated speed) is found in the definition of the saturation flux-linkage constant Ψ_s (i.e., where the line $D'B'$ crosses the vertical axis in Figure 7), resulting in

$$\Psi_s = V_{rms(PWM)}\frac{\beta_s}{\omega} - (L_{sa} - L_{uu})\frac{i_r}{c} \tag{11}$$

which when re-arranged (and substituting the values in Figure 7), becomes

$$V_{rms(PWM)} = \left(\Psi_s + (L_{sa} - L_{uu})\frac{i_r}{c}\right)\frac{\omega}{\beta_s} = \left(0.35575 + (0.0005 - 0.00043)\frac{320}{0.86}\right)\frac{125.7}{10.5} = 226V \tag{12}$$

Finally, all the information necessary to compute the co-energy W' is now available. Applying the above values to Eq.(6) gives

$$W' = \frac{1}{2}\left[2.(226)\frac{(0.86)(10.5)}{125.7}.(320) + \left(0.0005 - 0.00043\right)(320)^2 - \frac{\left(226\frac{(0.86)(10.5)}{125.7} + (0.0005 - 0.00043).320\right)^2}{0.0005 - 0.00043}\right] \approx 84J$$

Therefore, the electromagnetic torque and power [computed from Eq.(1)] becomes

$$T = 84\frac{(6)(12)}{2\pi} \times 1.0476 = 502.3Nm \qquad \text{giving} \qquad P = (502.3)(125.7) = 63126W$$

Computations of the above equations were also done for the case of the SRM2, and took into account the equivalent parameters and variables as defined previously in Table 2 [e.g., in line 21, the delta flux-linkage $\Psi(@B') - \Psi(@E') = 0.103378$ for the Dual-sided SyncRM is in fact $\Psi(@B) - \Psi(@D) = 0.081236$ for the SRM2 (in accordance to Figure 7)]. Note that some parameters are common to both motors. Figure 8 shows the computed speed-torque and speed-power characteristic curves [as per Qi et al (2019)] for both SRM2 and Dual-sided SyncRM. The later motor (Dual-sided SyncRM) shows an improvement performance, in that it can provide the original target SRM2 torque of $\sim 400N.m$ up to 1500rpm (higher than the original rated 1200rpm).

Efficiency is given as the ratio of produced electromagnetic power P_{em} to consumed average electric power P_{el}. The EM power has already been computed, and the average electric power $P_{el} = V_{av}.I_{av}$ is determined by analyzing the current (solid red lines in Figure 9) and voltage (solid blue lines in Figure 9) response as the rotor turns from the unaligned to aligned case. This then yields the average current I_{av} (dashed red line) and average voltage V_{av} (dashed blue line) for a complete rotational segment (from unalignment to alignment of rotor-to-stator poles). The flux-linkage characteristics can be converted into time periods of seconds (for each of the sectors in Figure 9) via the definition of Weber = V.s, in association with the applied voltages (i.e., which is either the Bus DC voltage V_{DC} or the root mean square rated voltage $V_{rms(PWM)}$) [the formulae and results are shown in the first half of Table 2 (lines 1-20)]. While the time periods t could also be converted into angles θ via the rotational speed ω (i.e., the average current and voltage could be computed either using angles or time intervals in the x-axis of Figure 9), the remainder of the calculation shall use time periods t. In Figure 9, the area bound by the polygon $\theta_{on}O'F'E'C'A'$ can be decomposed into 3 areas, namely that of the triangle $\triangle OC'A'(= A_{I1})$, the triangle $\triangle\theta_{on}OA'(= A_{I2})$ and the quadrilateral $\square OF'E'C'(= A_{I3})$. The first two are given as half the product of specific time intervals to the corresponding current levels, and are given as

$$A_{I1}(= A_{OC'A'}) = \frac{1}{2}\left\{(t_{A'C'})(i_r)\right\} = \frac{1}{2}\left\{\left(1.252 \times 10^{-3}\right)\left(320\right)\right\} = 0.2003A.s \tag{13}$$

and

$$A_{I2}(= A_{\theta_{on}OA'}) = \frac{1}{2}\left\{(t_{\theta_{on}A'})(i_r)\right\} = \frac{1}{2}\left\{\left(0.320 \times 10^{-3}\right)\left(320\right)\right\} = 0.512A.s \tag{14}$$

The third area requires the usage of vector theory again, this time to the quadrilateral $\square OF'E'C'$ (in Figure 9) that holds the vertices $(t_1, i_1) = (0, 0)$, $(t_2, i_2) = (t_{A'C'} + t_{E'F'} + t_{C'E'}, 0)$, $(t_3, i_3) = (t_{E'F'} + t_{C'E'}, i_s)$ and $(t_4, i_4) = (t_{A'C'}, i_r)$ [listed counterclockwise along its perimeter], giving the area

$$A_{I3}(= A_{OF'E'C'}) = \frac{1}{2}\left\{\left|\begin{array}{cc} t_{A'C'} + t_{E'F'} + t_{C'E'} & t_{E'F'} + t_{C'E'} \\ 0 & i_s \end{array}\right| + \left|\begin{array}{cc} t_{E'F'} + t_{C'E'} & i_s \\ t_{A'C'} & i_r \end{array}\right|\right\} \tag{15}$$

where the matrices in between the modulus are determinants, solved to be equal to the subtraction of the crossproducts.

Table 1. Computation of the EM torque and power for the SRM2 and Dual-sided SyncRM

Parameters	Variable [Dimensions]	SRM2	Dual-sided SyncRM	Source	Line
DC bus voltage	V_{DC} [V]	500		Input	1
Number of phases	q	3		Input	2
Stator (physical) poles	N_s	18		Input	3
Rotor (physical) poles	N_r	12		Input	4
Stator (magnetic) poles	N_m	6		Input	5
Rotations per minute	[rpm]	1200		Input	6
Frequency	f [Hz]	60		Eq.(7)	7
Rated angular speed	ω [rad/s]	125.7		Eq.(8)	8
Inductance					9
— Saturated aligned	L_{sa} [H]	0.00032	0.00043	Fig.(7)	10
— Unsaturated aligned	L_{ua} [H]	0.00644	0.00490	Fig.(7)	11
— (Unsaturated aligned @$i \leq 50A$)	(L^*_{ua}) [H]	(0.00737)	(0.00543)	Fig.(7)	12
— (Saturated aligned @$i \geq 120A$)	(L^*_{sa}) [H]	(0.00032)	(0.00043)	Fig.(7)	13
— Unsaturated unaligned	L_{uu} [H]	0.00109	0.0005	Fig.(7)	14
Aligned flux-linkage intercept	Ψ_S [V.s]	0.40456	0.35575	Fig.(7)	15
Saliency ratio					16
— (Unsaturated @$i \leq 50A$)	L^*_{ua}/L_{uu}	7	10		17
— (Saturated @$i \geq 120A$)	L^*_{sa}/L_{uu}	0.3	0.9		18
Rated current	i_r [A]	320		Input	19
Saturation current	i_s [A]	66.1	79.6	Eq.(5)	20
Flux-linkage @B'	$\Psi(@B')$ [V.s]	0.50717	0.49335	Fig.(7)	21
Flux-linkage @E'	$\Psi(@E')$ [V.s]	0.425934	0.389972	Fig.(7)	22
Delta flux-linkage	$\Psi(@B') - \Psi(@E')$	0.081236	0.103378		23
	[V.s]				24
Stator pole arc angle	β_s [deg]	10.5		Input	25
Rotation angle $C \to E$	θ_{CE} [deg]	1.17	1.49	Eq.(9)	26
Commutation factor	c	0.89	0.86	Eq.(10)	27
Rms voltage	$V_{rms(PWM)}$ [V]	87	226	Eq.(12)	28
Energy conversion capability	W' [J]	65	84	Eq.(6)	29
Overlap factor R		1.0476		Eq.(2)	30
Rated EM torque (recomputed)	T_{em} **[N.m]**	**390.5**	***502.3 (+29%)***	**Eq.(1)**	31
(experiments / predicted**)*		*(415 / 390)*			32
Rated EM power (recomputed)	P_{em} **[W]**	**49068**	**63126**	**Eq.(1)**	33
(experiments / predicted**)*		*(50kW / 49kW)*			34

*Takeno et al (2012) and **Stuikys and Sykulski (2020)*

Note that the first and fourth determinant in Eq.(15) are by definition 0 due to the origin vertice being null [i.e., $(x_1, y_1) = (0, 0)$]. Expanding and re-arranging [after some simplification] gives

$$A_{I3}(= A_{OF'E'C'}) = \frac{1}{2}\left\{(t_{E'F'} + t_{C'E'})(i_r + i_s)\right\} = \frac{1}{2}\left\{\left(0.780 \times 10^{-3} + 0.457 \times 10^{-3}\right)\left(320 + 68.3\right)\right\} = 0.2402A.s \tag{16}$$

In turn, the average current I_{av} equates to the ratio between the total sum of areas $\sum A_I = A_{I1} + A_{I2} + A_{I3}$ [in A.s] and the total amount of time [in seconds] taken during the trajectory path $\theta_{on}A'C'E'F'$ (these results are summarized in lines 21-26 of Table 2). The same procedure (done to compute the average current) can be applied to obtain the average voltage V_{av}. Finding the associated areas is simpler, as the profile of applied voltage (in blue) is square. Finally, the average voltage V_{av} equates to the ratio between the total sum of areas $\sum A_V$ [in V.s] and the total amount of time [in seconds]. Concluding, the Dual-sided SyncRM converts 69.3kW of average electric power into 63.1kW of electromagnetic power, resulting in an efficiency of 91% (at the rated operational speed of 1200 rpm). This is higher than the recomputed 75% efficiency of the SRM2 (against experiments estimation of 80% under rated torque and speed, and previous alternate numerical prediction of 72%), yielded by the conversion of 65.3kW of average electric power into 49.1kW of EM power (these results are summarized in lines 27-33 of Table 2).

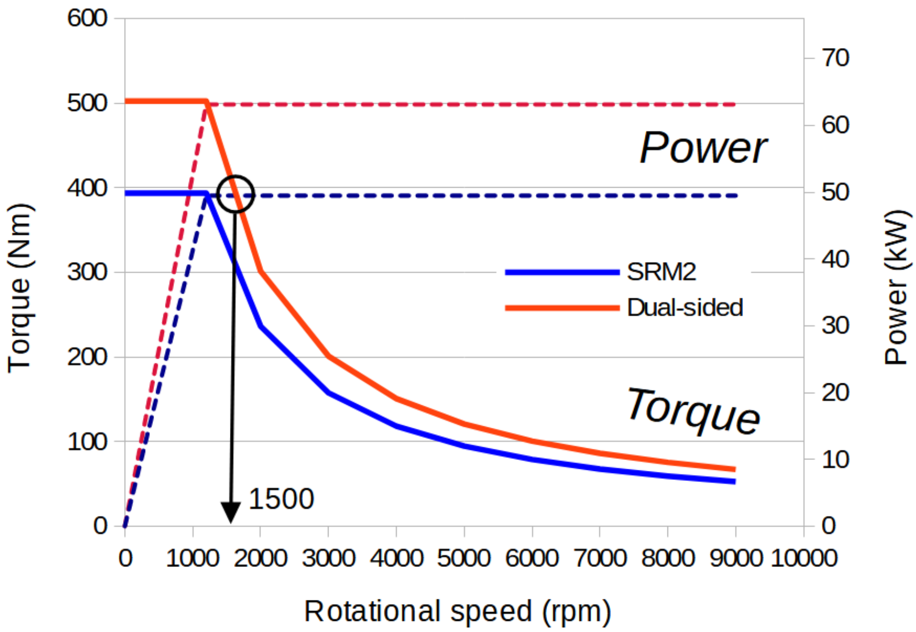

Figure 8: Speed-torque and speed-power characteristics of the SRM2 and Dual-sided SyncRM

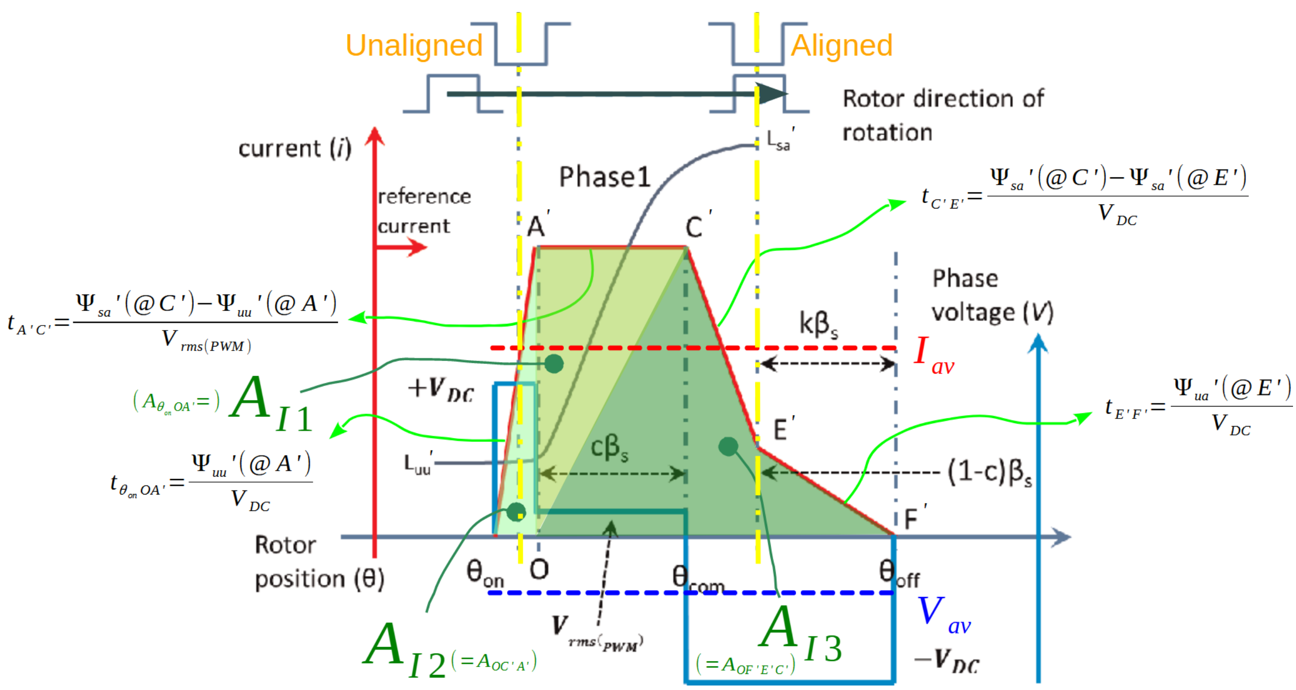

Figure 9: Current response as a function of voltage and rotor angular position [adapted from Stuikys and Sykulski (2020)]

5. Main Advantage

The main lesson learnt here is, that any torque dense SR motor needs to have the coils separated as much as possible from the larger part of the ferromagnetic material (except the blocks/poles around which they are winded around), to significantly minimize unaligned induction, thus maximizing saliency ratio. If a large chuck of ferromagnetic material remains attached to the stator (like it is typical in conventional SR motors, where the upper ring remains attached to the stator), during the unaligned state this will greatly conduct magnetic flux out of the coils, resulting in a large unwanted unaligned induction response, thus significantly reducing the induction torque (and power) conversion capability of the motor. This benefit (of decreasing the unaligned induction) by further splitting the stator (just above the coils, and reassigning this material to the rotor) largely outweighs the detriment (of decreasing the aligned induction) of adding another gap to the circuit. If this design change is incorporated, benefits of up to 29% in torque and power conversion can be achieved, as well as an efficiency boost up to 91% (at the rated operational speed of 1200rpm), in concentrated-coiled radial-flux synchronous reluctance motors.

Table 2. Efficiency computation for the SRM2 and Dual-sided SyncRM

Parameters	Variable [Dimensions]	SRM2	Dual-sided SyncRM	Source	Line
Flux-linkage	$\Psi_{uu}(@A')$ [V.s]	0.3488	0.4429	Fig. 7	1
DC bus voltage	V_{DC} [V]	500		Input	2
Time $\theta \to A'$	$t_{\theta A'}$ [s]	0.698×10^{-3}	0.320×10^{-3}	$\Psi_{uu}(@A')/V_{DC}$	3
		(18%)	*(11%)*		4
Delta flux-linkage	$d\Psi_1[V.s] =$	0.1131	0.2829	Fig. 7	5
	$= \Psi_{sa}(@C') - \Psi_{uu}(@A')$				6
Rms voltage	$V_{rms(PWM)}$ [V]	87	226	Eq.(12)	7
Time $A' \to C'$	$t_{A'C'}$ [s]	1.296×10^{-3}	1.252×10^{-3}	$d\Psi_1/V_{rms(PWM)}$	8
		(34%)	*(45%)*		9
Flux-linkage	$\Psi_{ua}(@E')$ [V.s]	0.4257	0.3900	Fig. 7	10
DC bus voltage	V_{DC} [V]	500		Input	11
Time $E' \to F'$	$t_{E'F'}$ [s]	0.851×10^{-3}	0.780×10^{-3}	$\Psi_{ua}(@E')/V_{DC}$	12
		(23%)	*(28%)*		13
Delta flux-linkages	$d\Psi_2[V.s] =$	0.081236	0.103378	Fig. 7	14
	$= \Psi(@C') - \Psi(@E')$				15
Rms voltage	$V_{rms(PWM)}$ [V]	87	226	Eq.(12)	16
Time $C' \to E'$	$t_{C'E'}$ [s]	0.931×10^{-3}	0.457×10^{-3}	$d\Psi_2/V_{rms(PWM)}$	17
		(25%)	*(16%)*		18
Total Time	t_T [s]	3.776×10^{-3}	2.809×10^{-3}	$\sum t$	19
		(100%)	*(100%)*		20
Area of $\triangle\theta_{on}OA'$	$A_{\theta_{on}OA'}$ [A.s]	0.3375	0.2003	Eq.(13)	21
Area of $\triangle OA'C'$	$A_{OA'C'}$ [A.s]	0.1116	0.0512	Eq.(14)	22
Rated current	i_r [A]	320		Input	23
Saturation current	i_s [A]	58.7	68.3	Input	24
Area of $\square OF'E'C'$	$A_{OF'E'C'}$ [A.s]	0.2073	0.2402	Eq.(16)	25
Total Area	A_{It} [A.s]	0.6565	0.4917	$\sum A$	26
Overlap factor R		1.0476		Eq.(2)	27
Average Current	I_{av} [A]	182	183	A_{It}/t_T	28
Average Voltage	V_{av} [V]	358	378	A_{Vt}/t_T	29
Average Electric Power	P_{el} [kW]	65.3	69.3	$P_{el} = I_{av}.V_{av}$	30
Electromagnetic Power	P_{em} [kW]	49.1	63.1	Eq.(1)	31
Efficiency	η	**75%**	**91%**	P_{em}/P_{el}	32
(experiments / predicted**)*		*(80% / 72%)*			33

*Takeno et al (2012) and **Stuikys and Sykulski (2020)

6. Conclusion

Two ways to enhance the electromagnetic torque, power output and efficiency of a synchronous reluctance motor are: (1) increasing the inductance of the magnetic circuits formed by the stator and rotor when aligned, or (2) reducing their inductance when they are unaligned. Both cases result in an increase of the (unsaturated) saliency ratio L_{ua}/L_{uu}. This article explores the second approach. It achieves this by partitioning the magnetic material of the stator, just radially outwards from the winding, and reassigned this to the rotor. By doing so, this change further minimizes the amount of magnetic material in contact with the coils during the unaligned case (i.e., reducing L_{uu}), boosting the co-energy W' and ultimately imparted an increase in reluctance torque (and electromagnetic power) by 29% of an existing SRM2 reluctance motor proposed to power the Toyota Yaris hybrid electric vehicle. Moreover, the conversion efficiency from electric to electromagnetic power raised to 91% with a saliency ratio of 10 (values applicable at the rated operational speed of 1200 rpm). This substantial performance improvement comes at the expense of a somewhat more mechanically intense (but achievable) machine to manufacture and assemble, with the final decision of advancing with such a modification resulting from a careful trade-off of performance gain versus mechanical complexity (encompassing what is acceptable as part of the project, within which this enhanced Dual-sided SyncRM is to be commercialized).

References

AKSteel. (2007). Selection of Electrical Steels for Magnetic Cores. *Technical datasheet*.

Arslan, B. I. (2021). *Learn Drafting with NanoCAD 5.0 (ECO Edition)*. Amazon.com

CADrays free software. (2023). Open Cascade Company. Retrieved from https://www.opencascade.com/products/cad-rays/

Guilera, L. C. (2018). *Analytical Design of a Synchronous Reluctance Motor*. Thesis: Escola Tècnica Superior d'Enginyeria Industrial de Barcelona.

Ionel, D. M., & Popescu, M. (2011). Finite-Element Surrogate Model for Electric Machines With Revolving Field — Application to IPM Motors. *IEEE Transactions on Industry Applications, 46*(6), 2424-2433. Retrieved from https://ieeexplore.ieee.org/document/5580086

Ladislav Knebl, L., Bianchi, N., Bacco, G., & Ondrusek, C. (2020). Synchronous Reluctance Motor Analytical Model Cross-saturation and Magnetization Analysis. *Przeglad Elektrotechniczny*. https://doi.org/10.15199/48.2020.01.24

Meeker D. Finite Element Method Magnetics (FEMM). *FEMM Reference Manual*. Retrieved from http://www.femm.info-/wiki/Documentation

Menzies, R. W. (1972). *Synchronous Reluctance Motors having Rotor Segments of Extended Pole Span*. Canadian Patents and Development Limited, U.S. Patent 3,671,789.

Misao, N., Hironori, N., & Tsunehiro, Y. (2005). High Silicon Steel Sheets Realizing Excellent High Frequency Reactor Performance. *JFE Technical Report*, No. 6.

NanoCAD free software. Retrieved from https://nanocad.com/products/nanocad-free

Qi, F., Scharfenstein, D., Weiss, C., Müller, C., & Schwarzer, U. (2019). *Motor Handbook*. Infineon Technologies AG, Institute for Power Electronics and Electrical Drives, RWTH Aachen University.

Shapiro, I. L., & de Berredo-Peixoto, G. (2013). *Lecture notes on Newtonian mechanics: Appendix A - Fundamentals of Vector Analysis*. Springer. Retrieved from https://catalogue.library.cern/literature/e15vm-vgn59

Stuikys, A., & Sykulski, J. (2020). Average Rated Torque Calculations for Switched Reluctance Machines Based on Vector Analysis. *IntechOpen Access Books*. http://dx.doi.org/10.5772/intechopen.89097

Takeno, M., Chiba, A., Hoshi, N., Ogasawara, S., Takemoto, M., & Rahman, M. A. (2012). Test results and torque improvement of the 50-kW switched reluctance motor designed for hybrid electric vehicles. *IEEE Transactions on Industry Applications, 48*(4), 1327-1334.

Wakisaka, T., Arai, S., & Kurosaki, Y. (2013). Electrical Steel Sheet for Traction Motor of Hybrid/Electrical Vehicles. *Nippon Steel Technical Report, 103*, 116-120. Retrieved from https://www.nipponsteel.com/en/tech/report/nsc/pdf/103-18.pdf

YouYou Technology Co. Ltd. (1993). JFE Super Core 10JNEX900/ 10JNHF600/ 10JNRF/ 15JNSF950. Technical data sheet. Retrieved from https://www.10jnex900.com/